Multifunctional three-dimensional macroporous nanoelectronic networks for smart materials

Multifunctional three-dimensional macroporous nanoelectronic networks for "smart" materials

Jia Liu[a,1], Chong Xie[a,1], Xiaochuan Dai[a,1], Lihua Jin[b], Wei Zhou[a] and Charles M. Lieber[a,b,2]

[a]Department of Chemistry and Chemical Biology, Harvard University, Cambridge, Massachusetts, 02138, [b]School of Engineering and Applied Sciences, Harvard University, Cambridge, Massachusetts, 02138

Author Contributions: J.L., C.X., X.D., and C.M.L. designed research. J.L., C.X., X.D., and W.Z. performed experiments and analyses. L.J. performed mechanics calculation J.L., C.X., X.D., and C.M.L. wrote the paper.

The authors declare no conflict of interest.

[1]J. L., C. X. and X. D. contributed equally to this work

[2]To whom correspondence should be addressed. E-mail: cml@cmliris.harvard.edu (C.M.L.)

This article contains supporting information.

Abstract: Seamless and minimally-invasive integration of three-dimensional (3D) electronic circuitry within host materials could enable the development of materials systems that are self-monitoring and allow for communication with external environments. Here, we report a general strategy for preparing ordered 3D interconnected and addressable macroporous nanoelectronic networks from ordered two-dimensional (2D) nanowire nanoelectronic "precursors", which are fabricated by conventional lithography. The 3D networks have porosities larger than 99%, contain ca. 100's of addressable nanowire devices, and have feature sizes from the 10 micron scale (for electrical and structural interconnections) to the 10 nanometer scale (for device elements). The macroporous nanoelectronic networks were merged with organic gels and polymers to form hybrid materials in which the basic physical and chemical properties of the host were not substantially altered, and electrical measurements further show a > 90% yield of active devices in the hybrid materials. The positions of the nanowire devices were located within 3D hybrid materials with ca. 14 nm resolution through simultaneous nanowire device photocurrent/confocal microscopy imaging measurements. In addition, we explored functional properties of these hybrid materials, including (*i*) mapping time-dependent pH changes throughout a nanowire network/agarose gel sample during external solution pH changes, and (*ii*) characterizing the strain field in a hybrid nanoelectronic elastomer structures subject to uniaxial and bending forces. The seamless incorporation of active nanoelectronic networks within 3D materials opens up a powerful approach to smart materials in which the capabilities of multi-functional nanoelectronics allow for active monitoring and control of host systems.

Keywords: nanowire/ 3D/ hybrid materials / smart systems

/body

Seamlessly merging functional electronic circuits in a minimally-invasive manner with host materials in 3D could serve as a pathway for creating "very smart" systems because this would transform conventional “inactive” materials into “active” systems. For example, embedded electronic sensor circuitry could monitor chemical, mechanical or other changes throughout a host material, thus providing detailed information about the host material’s response to external environments as well as desired feedback to the host and external environment (1, 2). Seamless and minimally-invasive integration of electronics in 3D has not been achieved except for our recent example of synthetic tissues (2). While focused on biological systems, this previous work provides key constraints for achieving our goal of a general strategy for integration electronic networks with host materials as follows. First, the addressable electronic networks must be macroporous, not planar, to enable 3D interpenetration with the host materials. Second, to minimize invasiveness of the macroporous electronic network it must have (*i*) microscale to nanoscale feature sizes, (*ii*) a small filling fraction with respect to the host (e.g., $\leq 1\%$), (*iii*) comparable or softer mechanical properties than the host, and (*iv*) an inert chemical response within the host material.

The constraints outlined above require the utilization of 3D nanoelectronic networks that are macroporous and have active elements (nanodevices). Two basic methods have been used to fabricate 3D integrated electronic circuits. The first involves bonding substrates, each containing devices/circuits integrated in 2D, together in a 3D stack (3, 4). The second exploits bottom-up assembly of nanoelectronic elements in a layer-by-layer manner (5-7). However, both methods yield solid or nonporous 3D structures that only allow the top-most layer of electronic elements to be merged directly with a second material and thus precluding integration of all of the

electronic elements seamlessly with a host material in 3D. Below, we describe a general strategy for 3D integration of electronics with host materials based on regular arrays of addressable nanowire nanoelectronic elements within 3D macroporous nanoelectronic networks, and also show how these networks can be used to map chemical and mechanical changes induced by the external environment in 3D.

Results and Discussion

We have focused on a bottom-up approach for realizing 3D macroporous nanoelectronic networks and their incorporation into host materials as outlined schematically in Figure 1. In this approach, we utilize functional nanowire nanoelectronic elements (Fig. 1*A*), where variations in composition, morphology and doping encoded during synthesis (8-14) define diverse functionality including devices for logic and memory (15, 16), sensors (17, 18), light-emitting diodes (10), and energy production and storage (19, 20). The macroporous nanoelectronic network with chosen nanowire elements (Fig. 1*B*) is realized through a combination of nanowire assembly and conventional 2D lithography carried out on a sacrificial substrate (see below); removal of the sacrificial layer yields free-standing and flexible 2D macroporous nanoelectronic networks (Fig. 1*B*). The 2D macroporous nanoelectronic networks are organized into 3D macroporous structures by either self- or directed-assembly, and then seamlessly merged within host material samples (Fig. 1*C*) using a solution (or liquid) -casting process at or near room-temperature.

The key steps involved in the fabrication, 3D organization and characterization of the macroporous nanoelectronic networks are outlined in Figure 2 (see *Materials and Methods*).

First, nanowires were uniaxially-aligned by contact printing (6, 21) on the surface of a layer of SU-8 negative resist, where the SU-8 was deposited by spin-coating on a Ni sacrificial layer deposited on a carrier substrate (Fig. 2*A, I*). Second, the SU-8 layer with aligned nanowires was patterned to define a periodic array by photolithography or electron beam lithography (EBL), and the excess nanowires on unexposed regions of the SU-8 were removed when the pattern was developed (Fig. 2*A, II*). The nanowire density and feature size in periodic arrays were chosen such that each element contained on average 1-2 nanowires. Third, a second SU-8 layer was deposited and patterned in a mesh structure by lithography (Fig. 2*A, III*). This SU-8 mesh serves to interconnect the nanowire/SU-8 periodic features and provides an adjustable support structure to tune the mechanical properties. Fourth, metal interconnects were defined by standard lithography and metal deposition on top of the appropriate regions of the SU-8 mesh, such that the end of nanowires were contacted and the nanowire elements were independently addressable (Fig. 2*A, IV*). Last, a third SU-8 layer was lithographically patterned to cover and passivate the metal interconnects.

Dark-field optical microscopy images obtained from a typical nanoelectronic mesh fabrication corresponding to the steps described above (Fig. 2*B, I-IV*) highlight several important features. First, the images recorded after contact printing (Fig. 2*B, I*) confirm that nanowires are well-aligned over areas where nanowire devices are fabricated. We can achieve good nanowire alignment on length scales up to at least several centimeters as reported elsewhere (6, 21). Second, a representative dark-field image of the patterned periodic nanowire regions (Fig. 2*B, II*) shows that this process removes nearly all of the nanowires outside of the desired features. Nanowires can be observed to extend outside of the periodic circular feature (i.e., an end is fixed at the feature) at some points; however, these are infrequent and do not affect subsequent steps

defining the nanodevice interconnections. Third, images of the underlying SU-8 mesh (Fig. 2*B*, *III*) and final device network with SU-8 passivated metal contacts and interconnects (Fig. 2*B*, *IV*) highlight the regular array of addressable nanowire devices realized in our fabrication process. Last, scanning electron microscopy (SEM) images (Fig. 2*C*) show that these device elements have on average 1-2 nanowires in parallel.

The 2D nanoelectronic mesh structures were converted to free-standing macroporous networks by dissolution of the sacrificial Ni layers over a period of 1-2 h (see *Materials and Methods*). Representative images of a free-standing nanoelectronic network (Fig. 2*D* and Fig. 2*E*) highlight the 3D and flexible characteristics of the structure and show how input/output (I/O) to the free-standing network can be fixed at one end outside of a solution measurement petri-dish chamber. Electrical characterization of individually-addressable nanowire device elements in a free-standing mesh demonstrates that the device-yield is typically ~90% (from 128 device design) for the free-standing nanoelectronic mesh structures fabricated in this way. The average conductance of the devices from a representative free-standing mesh (Fig. 2*F*), 2.85 ± 1.6 μS, is consistent with 1-2 nanowires/device based on measurements of similar (30 nm diameter, 2 μm channel length) p-type Si single nanowire devices (22), and thus also agrees with the structural data discussed above. In addition, by varying the printed nanowire density and S/D metal contact widths, it is possible to tune further the average number of nanowires per device element.

These 2D free-standing macroporous nanoelectronic networks were transformed to 3D structures using two general methods. First, 2D macroporous nanoelectronic networks were manually rolled-up into 3D arrays (Fig. 2*G*) with nanoelectronic elements in different layers of the resulting 'scroll' similar to our previous results for synthetic vascular structures (2). Second, by introducing built-in stress in metal interconnects with a trilayer metal stack (see *Materials and*

Methods) the mesh can be designed to self-organize into a similar scrolled structure as achieved by manual rolling. A reconstructed 3D confocal fluorescent image of a 3D nanoelectronic mesh array produced in this manner (Fig. 2*H*) shows clearly the 3D macroporous nanoelectronic network and can be used to estimate a free volume of (>99%). More generally, these self-organized 3D macroporous nanoelectronic structures could be readily diversified to meet goals for different hybrid materials using established mechanical design and bifurcation strategies (23).

Qualitatively, the facile manipulation of the macroporous nanoelectronic networks to form 3D structures suggests a very low effective bending stiffness. We have evaluated the effective bending stiffness, $\overline{D}$, using a combination of calculations and experimental measurements (see *SI text*, Figs. S2, S3). In short, $\overline{D} = \alpha_s D_s + \alpha_m D_m$ where D_s and D_m are bending stiffness per unit width for the SU-8 structural elements and SU-8/metal/SU-8 interconnects, respectively, and α_s and α_m are the respective area fractions for these elements in the networks. For typical 3D macroporous nanoelectronic networks, the area fraction for both types of elements (i.e., SU-8 and SU-8/metal/SU-8) can range from 1 –10%, yielding values of the effective bending stiffness from 0.0038 to 0.0378 nN-m.

The semiconductor nanowire elements can display multiple sensory functionalities, including photon (24), chemical, biochemical, and potentiometric (17, 22) as well as strain (25, 26) detection, which make them particularly attractive for preparing hybrid active materials as described below. We have first characterized photoconductivity changes (i.e., photon detection) of nanowire elements while imaging the nanoelectronic networks with a confocal microscope by recording conductance as a function of x-y-z coordinates and overlapping with simultaneously acquired fluorescence images (see *Materials and Methods*; Fig. 3*A* and Supplementary Fig. S4A). As the focused laser is scanned across a sample (Fig. 3*A, I*) an increase of conductance

due to the photocurrent (27) in nanowire is recorded at the positions of the nanowire devices. The resolution of this approach can be assessed in two ways. Conventionally, the plot of conductance versus position (Fig. *3A, II*) can be fit with a Gaussian function and its full-width at half-maximum (FWHM) reflects the diffraction limited resolution of the illuminating light spot. Second and recognizing that the nanowire diameter (30 nm) is line-like, we can use methods similar to super-resolution imaging technologies (28, 29) to locate the nanowire to much higher precision by identifying the peak position from the Gaussian fit. We note that a similar concept as exploited in stochastic super-resolution imaging to resolve close points can be implemented in our photoconductivity maps because individual devices can be turned on and off as needed (28).

A typical high-resolution photoconductivity image of a single nanowire device (Fig. 3*B, I*) shows clearly the position of the nanowire. The conductance change versus x-position perpendicular to the nanowire axis (Fig. 3*B, II* and Supplementary Fig. S4B) yielded a FWHM is 314 ± 32 nm (n = 20) resolution consistent with confocal microscopy imaging resolution (202 nm) in this experiment. Moreover, the nanowire position determined from the peaks of Gaussian fits (Supplementary Fig. S4C) yielded a standard deviation of 14nm (n = 20), and shows that the position of devices can be localized with a precision better than the diffraction limit. In addition, we have acquired simultaneous photoconductivity and fluorescence confocal microscopy images to map the positions of nanowire devices in 3D macroporous nanoelectronic networks. Reconstructed 3D images (Fig. 3*C*) show that the 12 active nanowire devices can be readily mapped with respect to x-y-z coordinated in the 'rolled-up' macroporous nanoelectronic network structure. Given the complexity possible in 3D nanoelectric/host hybrid materials, this approach provides straightforward methodology for determining at high-resolution the positions of the active nanoelectronic sensory elements with respect to structures within the host. In the future,

we also note that the resolution could be even further improved by incorporating point-like transistor photoconductivity detectors (17, 30), p-n photodiodes (31) and p-i-n avalanche photodiodes (32) nanowire building blocks within the 3D macroporous nanoelectronic network.

Second, we have used macroporous nanowire nanoelectronic networks to map pH changes in 3D through agarose gel using a macroporous nanoelectronic/gel hybrid, and for comparison, in aqueous solution using a free-standing 3D nanoelectronic sensory network. The hybrid nanoelectronic/gel material was prepared by casting the agarose around a rolled-up macroporous nanoelectronic network, where the gel and SU-8 mesh of the nanoelectronic network were doped with 4',6-diamidino-2-phenylindole (DAPI) and rodamine 6G, respectively (see *Materials and Methods*). A reconstructed 3D confocal microscopy image of the hybrid material (Fig. 4*A*) shows clearly the 3D device mesh fully embedded within an agarose gel block without phase separation. To carry out sensing experiments either the 3D nanoelectronic/gel hybrid material or a 3D nanoelectronic mesh was contained within a microfluidic chamber (Fig. 4*B*). Positions of nanowire transistor devices, which can function as very sensitive chemical/biological detectors (17, 22, 33), were determined by the photocurrent mapping method described above. For both 3D nanoelectronic mesh and nanoelectronic/gel hybrid we recorded signals simultaneously from 4 devices chosen to span positions from upper to lower boundary of mesh or gel, where representative z-coordinates of the devices positions within the hybrid sample are highlighted in Fig. 4*C*; a similar z-range of devices for the free nanoelectronic mesh was also used.

Representative data recorded from p-type nanowire FET devices in 3D mesh network without gel (Fig. 4*D, I*) and in the hybrid 3D nanoelectronic mesh/agarose gel hybrid (Fig. 4*D, II*) highlight several important points. First, the device within 3D macroporous network without

gel showed fast stepwise conductance changes (<1 s) with solution pH changes. The typical sensitivity of these devices was ca. 40 mV/ pH, and is consistent with values reported for similar nanowire devices (18). Second, the device within the 3D nanoelectronic mesh/gel hybrid exhibited substantially slower transition times with corresponding changes of the solution pH; that is, signal change required on order of 2000 s to reach steady-state, and thus was 1000-fold slower than in free solution. Third, the device within the 3D nanoelectronic mesh/gel hybrid exhibited lower pH sensitivity in terms of mV/pH; that is, 20 - 40 mV/pH for device in gel compared to 40 - 50 mV/pH for device in free solution.

Direct comparison of the temporal responses of four devices at different 3D positions in the two types of samples (Fig. 4*E*) provides additional insight into the pH changes. The time to achieve one-half pH unit change for the four different devices in 3D macroporous network without gel (Fig. 4*E, I*) is ca. 0.5 s and the difference between devices is only ca. 0.01 s. We note that the time delay in the data recorded from device d4 is consistent with the down-stream position of this device within the fluidic channel. In contrast, the time to achieve one-half for the four devices in the 3D nanoelectronic mesh/gel hybrid (Fig. 4*E, II*) range from ca. 280 to 890s for devices d1 to d4, respectively, where devices positions are shown in Fig. 4*C*. The results show that the device response time within the agarose is ca. 500 – 1700 times slower than in solution and is proportional to the distance from the solution/gel boundary, although the detailed variation suggests heterogeneity in the diffusion within the agarose gel. Significantly, the ability to map the diffusion of molecular and biomolecular species in 3D hybrid systems using the macroporous nanoelectronic sensory networks offers opportunities for self-monitoring of gel, polymers and tissue systems relevant to many areas of science and technology (34, 35).

Third, we have used embedded 3D macroporous nanoelectronic networks to map strain distributions in elastomeric silicone host materials. Previous studies have shown that Si nanowires have a high piezoresistance response (25), making them good candidates for strain sensors (26). To explore the potential of Si nanowire device arrays to map strain within materials, we have prepared and characterized 3D macroporous nanoelectronic network/elastomer hybrid materials (see *Materials and Methods*). The resulting hybrid macroporous nanoelectronic network/elastomer cylinders had volumes of ca. 300 mm^3 with volume ratio of device/elastomer of < 0.1%. X-ray micro-computed tomography (μCT) studies of the nanoelectronic network/elastomer cylinders (Fig. 5*A* and Supplementary Fig. S5) were used to determine the 3D metal interconnects and locations of nanowire devices within the cylindrical hybrid structures (see *Materials and Methods*). The alignment of nanowire elements along the cylinder axis was confirmed by dark-field optical microscopy images (Fig. 5*B*), which show the nanowires lying along the cylinder (z) axis.

The good axial alignment of the nanowire devices was exploited to calibrate the strain sensitivity of each of elements with the 3D hybrid structure allows straightforward calibration of the device sensitivity in pure tensile strain field. Application of a 10% tensile strain along the cylinder axis (Supplementary Fig. S5A) yielded decreases in conductance up to 200 nS for the individual devices, d1 – d11. Because the conductance immediately returned to baseline when strain was released and under compressive loads the conductance change had the opposite sign, we can conclude that these changes do reflect strain transferred to the nanowire sensors. From the specific response of the devices within the hybrid structure we calculate and assign a calibrated conductance change/1% strain value for each of the eleven sensor elements (Supplementary Fig. S5), and use this for analysis of different applied strains. For example, we

applied a bending strain to the cylinder and from the recorded conductance changes and calibration values were able to map readily the 3D strain field as shown in Fig. 5*C*. We note that the one-dimensional geometry of nanowires gives these strain sensors nearly perfect directional selectivity, and thus, by developing macroporous nanoelectronic network with nanowires device aligned parallel and perpendicular to the cynlinder axis enable mapping all three components of the strain field in the future. .

Conclusions

We have demonstrated a general strategy for preparing ordered 3D interconnected and addressable macroporous nanoelectronic networks from ordered 2D nanowire nanoelectronic "precursors", which are fabricated by conventional lithography. The 3D networks have porosities larger than 99%, contain 100's of addressable nanowire devices, and have feature sizes from the 10 micron scale for electrical and structural interconnections to the 10 nanometer scale for the functional nanowire device elements. The macroporous nanoelectronic networks were merged with organic gels and polymers to form hybrid materials in which the basic physical and chemical properties of the host were not substantially altered, and electrical measurements further show > 90% yield of active devices in the hybrid materials. We further demonstrated a new approach to determine the positions of the nanowire devices within 3D hybrid materials with ca. 14 nm resolution that involves simultaneous nanowire device photocurrent/confocal microscopy imaging measurements. This method also could have substantial impact on localizing device positions in macroporous nanoelectronic/biological samples, where it provides the capability of determining positions of sensory devices at the subcellular level. In addition, we explored functional properties of these hybrid materials. First, we showed that it was possible to

map time-dependent pH changes throughout a nanowire network/agarose gel sample during external solution pH changes. These results suggest substantial promise of the 3D macroporous nanoelectronic networks for real-time mapping of diffusion of chemical and biological species through polymeric samples as well as biological materials such as synthetic tissue (34, 36). Second we demonstrated that Si nanowire elements can function as well-defined strain sensors, and thereby characterize the strain field in a hybrid nanoelectronic elastomer structures subject to uniaxial and bending forces. More generally, we believe our approach to fabrication of multi-functional 3D electronics and integration with host materials suggests substantial promise for (*i*) general fabrication of truly 3D integrated circuits based on conventional fabrication processes via assembly from a 2D "precursor", (*ii*) seamless 3D incorporation of multi-functional nanoelectronics into living and nonliving systems leading to make "very smart" material systems and a completely new level of "cyborg" tissues.

Materials and Methods.

1. Nanowire Synthesis.

Single-crystalline nanowires were synthesized using the Au nanocluster-catalyzed vapor-liquid-solid growth mechanism in a home-built chemical vapor deposition (CVD) system described previously (37). Au nanoclusters (Ted Pella Inc., Redding, CA) with 30 nm diameters were dispersed on the oxide surface of silicon/SiO_2 substrates (600 nm oxide) and placed in the central region of a quartz tube CVD reactor system. Uniform 30 nm *p*-type silicon nanowires were synthesized using reported methods (37). In a typical synthesis, the total pressure was 40 torr and the flow rates of SiH_4, diborane (B_2H_6, 100 p.p.m. in H_2), and hydrogen (H_2, Semiconductor Grade), were 2, 2.5 and 60 standard cubic centimetres per minute (SCCM), respectively. The silicon-boron feed-in ratio was 4000:1, and the total nanowire growth time was 30 min.

2. 3D macroporous nanoelectronic networks.

The 3D macroporous nanowire nanoelectronic networks was initially fabricated on the oxide or nitride surfaces of silicon substrates (600nm SiO_2 or 100 SiO_2/200 Si_3N_4, *n*-type 0.005 V·cm, Nova Electronic Materials, Flower Mound, TX) prior to relief from the substrate. Key steps used in the fabrication of the 3D macroporous nanowire nanoelectronic networks were as follows: (*i*) lithography and thermal deposition were used to pattern a 100 nm nickel metal layer, where the nickel served as the final relief layer for the 2D free-standing macroporous nanowire nanoelectronic networks. (*ii*) A 300-500 nm layer of SU-8 photoresist (2000.5, MicroChem Corp., Newton, MA) was deposited over the entire chip followed by pre-baking at 65 ^{o}C and 95 ^{o}C for 2 and 4 min, respectively, then (*iii*) the synthesized nanowires were directly printed from growth wafer over the SU-8 layer by the contact printing methods reported previously. (*iv*) Lithography (photolithography or electron beam lithography) was used to define regular patterns

on the SU-8. After post-baking (65 ^{o}C and 95 ^{o}C for 2 and 4 min, respectively), SU-8 developer (MicroChem Corp., Newton, MA) was used to develop the SU-8 pattern. Those areas exposed to UV light or electron beam became dissolvable to SU-8 developer and other areas were dissolved by SU-8 developer. Those nanowires on the non-exposed area will be removed by further washing away in isopropanol solution (30 s) for twice leaving those selected nanowires on the regular pattern SU-8 structure. The SU-8 patterns were curing at 180 ^{o}C for 20 min. (*v*) A 300-500 nm layer of SU-8 photoresist was deposited over the entire chip followed by pre-baking at 65 ^{o}C and 95 ^{o}C for 2 and 4 min, respectively. Then lithography was used to pattern the bottom SU-8 layer for passivating and supporting the whole device structure. The structure was post-baked, developed and cured by the same procedure as described above. (*vi*) Lithography and thermal deposition were used to define and deposit the metal contact to address each nanowire device and form interconnections to the input/output pads for the array. For the mesh device, in which the metal is non-stressed, symmetrical Cr/Pd/Cr (1.5/50-80/1.5 nm) metal was sequentially deposited followed by metal lift-off in acetone. For the self-organized networks, in which the metal are stressed, nonsymmetrical Cr/Pd/Cr (1.5/50-80/50-80 nm) metal was sequentially deposited followed by metal lift-off in acetone. (*vii*) A 300-500 nm layer of SU-8 photoresist was deposited over the entire chip followed by pre-baking at 65 ^{o}C and 95 ^{o}C for 2 and 4 min, respectively. Then lithography was used to pattern the top SU-8 layer for passivating the whole device structure. The structure was post-baked, developed and cured by the same procedure as described above. (*viii*) The 2D macroporous nanowire nanoelectronic networks was released from the substrate by etching of the nickel layer (Nickel Etchant TFB, Transene Company Inc., Danvers, MA) for 60-120 min at 25 ^{o}C. (*ix*) The 3D macroporous nanowire

nanoelectronic networks were dried by a critical point dryer (Autosamdri 815 Series A, Tousimis, Rockville, MD) and stored in the dry state prior to use.

3. Characterization of macroporous nanoelectronic networks.

Scanning electron microscopy (SEM, Zeiss Ultra55/Supra55VP field-emission SEMs) was used to characterize the macroporous nanoelectronic networks. Bright-field and dark-field optical micrographs of samples were acquired on an Olympus FSX100 system using FSX-BSW software (ver. 02.02). Fluorescence images of the 3D macroporous nanoelectronic networks were obtained by doping the SU-8 resist solution with Rhodamine 6G (Sigma-Aldrich Corp., St. Louis, MO) at a concentration less than 1 μg/mL before deposition and patterning. *ImageJ* (ver. 1.45i, Wayne Rasband, National Institutes of Health, USA) was used for 3D reconstruction and analysis of the confocal and epi-fluorescence images. Bending stiffness of the SU-8/metal/SU-8 ribbon is measured using an Asylum MFP-3D AFM system. An AFM tip with calibrated k of 9.7 nN/nm is used.

4. Electrical measurement of 3D macroporous nanoelectronic networks.

NW device recording was carried out with a 100 mV DC source voltage, and the current was amplified with a home-built multi-channel current/voltage preamplifier with a typical gain of 10^6 A/V. The signals were filtered through a home-built conditioner with band-pass of 0-3 kHz, digitized at a sampling rate of 20 kHz (Axon Digi1440A) and recorded using Clampex 10 software (MDS)

5. 3D macroporous photodetectors and device localization in 3D.

Confocal laser scanning microscopy (Fluoview FV1000, Olympus America Inc., PA) was used to characterize the 3D macroporous nanoelectronic network. Conventional 405 nm and 473 nm wavelength lasers, where 405 nm was used to produce photocurrents in the nanowire transistor

devices, and the 473 nm was used for fluorescence imaging. The SU-8 structure was doped with Rodamine 6G for fluorescence imaging. The macroporous nanoelectronic network was immersed into dioniozed (DI) water, individual devices were biased with 100 mV, and 40X or 100X water immersion objectives were used for imaging. The photocurrent signal was amplified (SIM 918, Stanford Research System, MA) bandpass filtered, (1-6000 Hz, home-built system), and synchronized with laser scanning position using an analog signal input box (F10ANALOG, Olympus America Inc., PA). The conductance signal from the resulting images was read out by *imageJ*, and the data were analyzed and fitted by *OriginPro*.

6. 3D macroporous chemical sensors.

Agarose (Sigma) was dissolved into DI water and made as 0.5%, and heated up to 100 ^{o}C. The gel was drop casting onto the device and cooled down to room temperature. 4',6-diamidino-2-phenylindole (DAPI, Sigma) was used to dope the gel for the confocal 3D reconstructed imaging. A PDMS fluidic chamber with input/output tubing and Ag/AgCl electrodes was sealed with the silicon substrate and the device or device-gel hybrid using silicone elastomer glue (Kwik-Sil, World Precision Instruments, Inc). Fresh medium was delivered to the device region through both inner and outer tubing. The solution pH was stepwise varied inside the channel by flowing (20 mL/h) 1x phosphate buffered solutions with fixed pH values from pH 6-8. The recorded device signals were filtered with a bandpass filter of 0-300 Hz.

7. 3D macroporous strain sensors in elastomer.

A freestanding 2D macroporous nanoelectronic network was suspended in water, and placed on a thin (200 – 500 μm) piece of cured silicone elastomer sheet (Sylgard 184, Dow Corning). The hybrid macroporous nanowire network/silicon elastomer was rolled into a cylinder, infiltrated with uncured silicone elastomer under vacuum, and cured at 70°C for 4 hours. The resulting

hybrid nanoelectronic/elastomer cylinders had volumes of ca. 300 mm^3 with volume ratio of device/elastomer of < 0.1%. The structure of the macroporous electronics/elastomer hybrid was determined using a HMXST X-ray micro-CT system with a standard horizontal imaging axis cabinet (model: HMXST225, Nikon Metrology, Inc., Brighton, MI). In a typical imaging experiment, the acceleration voltage was 60-70 kV, the electron beam current was 130-150 mA, and no filter was used. *BGStudio* MAX (ver. 2.0, Volume Graphics GMbh, Germany) was used for 3D reconstruction and analysis of the micro-CT images, which resolve the 3D metal interconnect structure and nanowire S/D contacts; the Si nanowires were not resolved in these images but were localized at the scale of the S/D contacts. The piezoelectric response to strain of the nanowire devices was calibrated using a mechanical clamp device under tensile strain (Supplementary Fig. S5), where the strain was calculated from the length change of the cylindrical hybrid structure. The bending strain field was determined in experiments where the the cylindrical hybrid structure, with calibrated nanowire strain sensors, was subject to random bending deflections.

Acknowledgments

We thank B. Tian and M. Ji for helpful discussions. This study was supported by NIH Director's Pioneerand NSSEFF awards (C.M.L.).

References

1. Reuss RH, Hopper DG, Park JG (2006) Macroelectronics. *MRS Bulletin* 31:447-454.
2. Tian B, et al. (2012) Macroporous nanowire nanoelectronic scaffolds for synthetic tissues. *Nature Mater* 11: 986-994.
3. Al-sarawi SF, Abbott D, Franzon PD (1998) A review of 3-D packaging technology. *IEEE Trans Components Pag & Manuf Technol* 21: 2-14.
4. Benkart P, et al. (2005) 3D chip stack technology using through-chip interconnects. *IEEE Des Test Comput* 22:512-518.
5. Ahn JH, et al. (2006) Heterogeneous three-dimensional electronics by use of printed semiconductor nanomaterials. *Science* 314:1754-1757.
6. Javey A, Nam S, Friedman RS, Yan H, Lieber CM (2007) Layer-by-layer assembly of nanowires for three-dimensional, multifunctional electronics. *Nano Lett* 7:773-777.
7. Nam S, Jiang X, Xiong Q, Ham D, Lieber CM (2009) Vertically integrated, three-dimensional nanowire complementary metal-oxide-semiconductor circuits. *Proc Natl Acad Sci USA* 106:21035-21038.
8. Lu W, Lieber CM (2007) Nanoelectronics from the bottom up. *Nature Mater* 6:841-850.
9. Lieber CM, Wang ZL (2007) Functional nanowire. *MRS Bull* 32:99-104.
10. Qian F, Gradecak S, Li Y, Wen Y, Lieber CM (2005) Core/multishell nanowire heterostructures as multicolor, high-efficiency light-emitting diodes. *Nano Lett* 5:2287-2291.
11. Tian B et al. (2007) Coaxial silicon nanowires as solar cells and nanoelectronic power sources. *Nature* 449:885-890.

12. Tian B, Xie P, Kempa TJ, Bell DC, Lieber CM (2009) Single-crystalline kinked semiconductor nanowire superstructures. *Nature Nanotechnol* 4:824-829.

13. Gao R et al. (2012) Outside looking in: Nanotube transistor intracellular sensors. *Nano Lett* 12:3329-3333.

14. Jiang X et al. (2011) Rational growth of branched nanowire heterostructures with synthetically encoded properties and function. *Proc. Natl. Acad. Sci. USA* 108:12212-12216.

15. Yan H et al. (2011) Programmable nanowire circuits for nanoprocessor. *Nature* 470:240-244.

16. Xiang J, et al. (2006) Ge/Si nanowire heterostructures as high-performance field-effect transistors. *Nature* 441:489-493.

17. Cui Y, Wei Q, Park H, Lieber CM (2001) Nanowire nanosensors for highly sensitive and selective detection of biological and chemical species. *Science* 293:1289-1292.

18. Tian B, et al. (2010) Three-dimensional, flexible nanoscale field-effect transistors as localized bioprobes. *Science* 329:831-834.

19. Qin Y, Wang XD, Wang ZL (2008) Microfiber-nanowire hybrid structure for energy scavenging. *Nature* 451:809-813.

20. Chan CK, et al. (2008) High performance lithium battery anodes using silicon nanowires. *Nature Nanotechnol* 3:31-35.

21. Fan ZY et al. (2008) Wafer-scale assembly of highly ordered semiconductor nanowire arrays by contact printing. *Nano Lett* 8:20-25.

22. Zheng G, Patolsky F, Cui Y, Wang WU, Lieber CM (2005) Multiplexed electrical detection of cancer markers with nanowire sensor arrays. *Nature Biotechnol* 23:1294-1301.

23. Freund LB (2000) Substrate curvature due to thin film mismatch strain in the nonlinear deformation range. *J Mech Phys Solids* 48:1159-1174.

24. Fan Z, Ho JC, Jacobson ZA, Razavi H, Javey A (2008) Large-scale, heterogeneous integration of nanowire arrays for image sensor circuitry. *Proc Natl Acad Sci USA* 105:11066-11070.

25. He R, Yang P (2006) Giant piezoresistance effect in silicon nanowires. *Nature Nanotechnol* 1:42-46.

26. Lee CH, Kim DR, Zheng X (2009) Fabricating nanowire devices on diverse substrates by simple transfer-printing methods. *Proc Natl Acad Sci USA* 107:9950-9955.

27. Tsen AW, Donev LAK, Kurt H, Herman LH, Park J (2009) Imaging the electrical conductance of individual carbon nanotubes with photothermal current microscopy. *Nature Nanotechnol* 4:108-113.

28. Huang B, Wang WQ, Bates M, Zhuang XW (2008) Three-dimensional super-resolution imaging by stochastic optical reconstruction microscopy. *Science* 319:810-813.

29. Toprak E, Balci H, Blehm BH, Selvin PR (2007) Three-dimensional particle tracking via bifocal imaging. *Nano Lett* 7:2043-2045.

30. Cohen-Karni T et al. (2012) Synthetically encoded ultrashort-channel nanowire transistors for fast, pointlike cellular signal detection. *Nano Lett* 12:2639-2644.

31. Jiang Z, Qing Q, Xie P, Gao R, Lieber CM (2012) Kinked p-n junction nanowire probes for high spatial resolution sensing and intracellular recording. *Nano Lett* 12:1711-1716.

32. Hayden O, Agarwal R, Lieber CM (2006) Nanoscale avalanche photodiodes for highly sensitive and spatially resolved photon detection. *Nature Mater* 5:352-356.

33. Patolsky F, Timko BP, Zheng G, Lieber CM (2007) Nanowire-based nanoelectronic devices in the life science. *MRS Bulletin* 32:142-149.

34. Griffith LG, Swartz MA (2006) Capturing complex 3D tissue physiology *in vitro*. *Nature Rev Mol Cell Biol* 7:211-224.

35. Sanger F (1977) DNA sequencing with chain-terminating inhibitors. *Proc Natl Acad Sci USA* 74:5463-5467.

36. Glicklis R, Merchuk JC, Cohen S (2004) Modeling mass transfer in hepatocyte spheroids via cell viability, spheroid size, and hepatocellular functions. *Biotechnol. Bioeng*. 86:672-680.

37. Patolsky F, Zheng G, Lieber CM (2006) Fabrication of silicon nanowire devices for ultrasensitive, label-free, real-time detection of biological and chemical species. *Nature Protocol* 1:1711-1724.

Figure Legends

Fig. 1. Strategy for preparing 3D macroporous nanoelectronic networks and integration with host materials. (*A*) Different nanowire nanoelectronic elements (*from left to right*): kinked nanowire, nanotube, core-shell, straight and branched nanowire. (*B*) Free-standing 2D macroporous nanowire nanoelectronic "precursor". Blue: nanoelectronic element, orange: passivation polymer, black: metal contact and input/output (I/O). (*C*) 3D macroporous nanoelectronic networks integrated with host materials (*Gray*).

Fig. 2. Organized 2D and 3D macroporous nanoelectronic networks. (*A*) Schematics of nanowire registration by contact printing and SU-8 patterning. Gray: Silicon wafer, blue: Ni sacrificial layer, black ribbon: nanowire, green: SU-8, red: metal contact. (*Top*) shows top view and (*bottom*) shows side view. (*I*): Contact printing nanowire on SU-8. (*II*): Regular SU-8 structure was patterned by lithography to immobilize nanowires. Extra nanowires were washed away during the develop process of SU-8. (*III*): Regular bottom SU-8 structure was patterned by spin-coating and lithography. (*IV*): Regular metal contact was patterned by lithography and thermal evaporation, followed by top SU-8 passivation. (*B*) Dark field optical images corresponding to each step of schematics in (*A*). The nanowire and SU-8 features appear green in these images. The small red features on the right and lower edges of the image in (*II*) correspond to metal lithography markers used in alignment. The red dashed line highlights metal contacts/interconnects in (*IV*). (*C*) SEM image of a 2D macroporous nanoelectronic network prior to release from the substrate. *Inset*, corresponds to zoom-in of the region enclosed by the red dashed box containing a single nanowire device. (*D*) Photograph of wire-bonded free-

standing 2D macroporous nanoelectronic network in petri-dish chamber for aqueous solution measurements. The red dashed box highlights the free-standing portion of the nanoelectronic network and the white-dashed box encloses the wire-bonded interface between the input/output (I/O) and PCB connector board. (*E*) Zoom-in of the region enclosed by the red-dashed box in (*D*). (*F*) Histogram nanowire device conductance in the free-standing 2D macroporous nanoelectronic networks. (*G*) Photograph of a manually scrolled-up 3D macroporous nanoelectronic network. (*H*) 3D reconstructed confocal fluorescence images of self-organized 3D macroporous nanoelectronic network viewed along the x-axis. Nonsymmetrical Cr/Pd/Cr metal layers (see *Materials and Methods*), which are stressed, were used to drive self-organization. The SU-8 ribbons were doped with Rodamine-6G for imaging.

Fig. 3. 3D macroporous photodetectors and device localization. (*A*) Schematics of the single 3D macroporous nanowire photodetector characterization. The green ellipse: laser spot, blue cylinder: nanowire and orange: SU-8 mesh network. The illumination of the laser spot generated from confocal microscope on the nanowire device (*I*) makes the conductance change of nanowire, which could be (*II*) correlated with laser spot position. Green spots in (*II*) correlate to the laser spot positions in (*I*). (*B*) High-resolution (1 nm per pixel) photocurrent image (*I*) from single nanowire device (2 μm channel length) on substrate recorded with focused laser spot scanned in x-y plane. The black dash lines indicate the boundary of metal contact in the device.(*II*) 20 times photocurrent measurements from the central region (red dash box) of the nanowire device with high resolution (the distance for each trace in x-direction is 1 nm). (*C*) 3D reconstructed photocurrent imaging overlapped with confocal microscopy imaging shows the spatial correlation between nanowire photodetectors with SU-8 framework in 3D. Green: false

color of the photocurrent signal, orange (rhodamine 6G): SU-8 mesh network. Dimensions in (*I*), x: 317 μm; y: 317 μm; z: 53 μm; in (*II*), x: 127 μm; y: 127 μm; z: 65 μm. The white numbers in (*II*) indicate the heights of the nanowire photodetectors.

Fig. 4. 3D macroporous chemical sensors. (*A*) x-z views of 3D reconstructed image of the 3D macroporous nanoelectronic network in gel. Red (rhodamine 6G): SU-8 mesh network and blue (DAPI): agrose gel. Dimensions: x = 317 μm; y = 317 μm; and z = 144 μm. (*B*) Schematics of the experimental set-up. (*C*) The projection of four nanowire devices in the y-z plane. Red dashed line corresponds to the approximate gel boundary, and the red and blue areas correspond to aqueous solution and agrose gel, respectively. (*D*) Representative change in calibrated voltage over time with pH change for 3D macroporous nanowire chemical sensors (*I*) in solution (*I*) and (*II*) embedded in agrose gel. (*E*) Calibrated voltage with one pH value change in solution for 4 different devices located in 3D space. (*I*) 4 devices without gel and (*II*) 4 devices embedded in agrose gel.

Fig. 5. 3D macroporous strain sensors embedded in elastomer. (*A*) μCT 3D reconstruction of the macroporous strain sensor array embedded in a piece of elastomer. Pseudo-colors are applied: orange: metal, purple: elastomer. (*B*) Dark field microscopy image of a typical nanowire device indicated by red dash circle in (*A*). All the functional nanowires are intentionally aligned parallel to the axial axis of the elastomer cylinder. The white arrow points a nanowire. (*C*) A bending strain field was applied to the elastomer piece. The 3D strain field was mapped by the nanowire strain sensors using the sensitivity calibration of the nanowire devices. The detected strains are labeled in the cylinder image at the device positions.

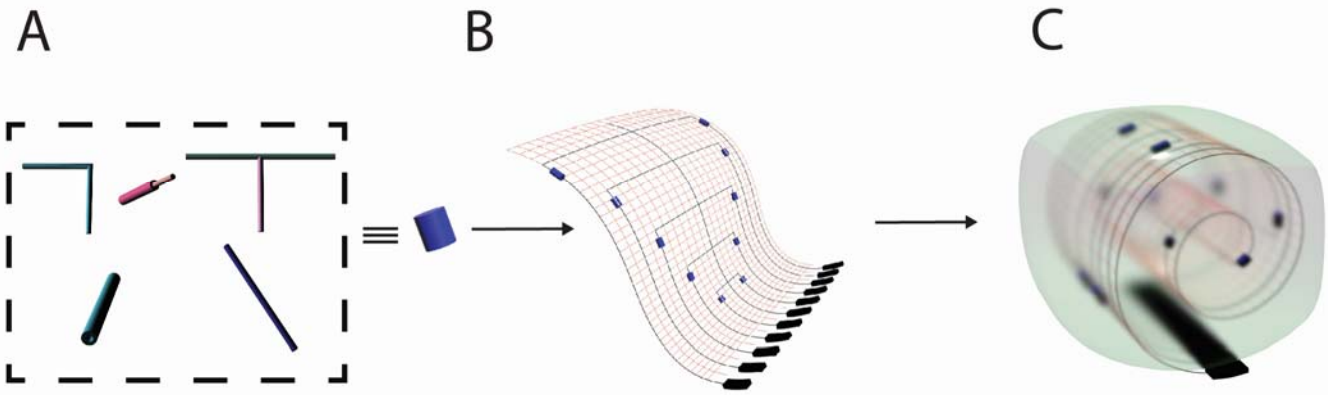

Figure 1

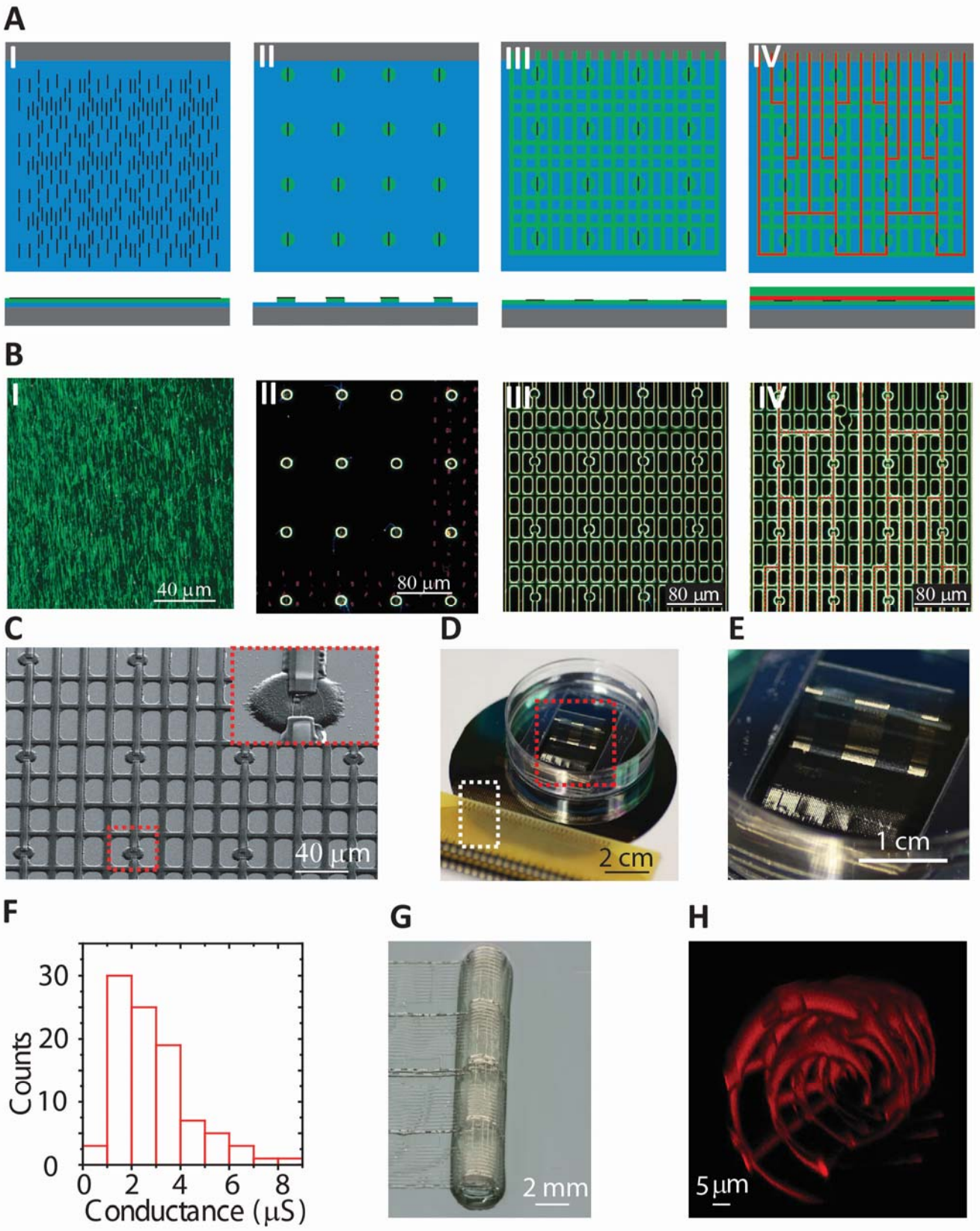
A
I
II
III
IV
B
I
40 µm
II
80 µm
III
80 µm
IV
80 µm
C
40 µm
D
2 cm
E
1 cm
F
30
20
10
0
Counts
0
2
4
6
8
Conductance (µS)
G
2 mm
H
5 µm

Figure 2

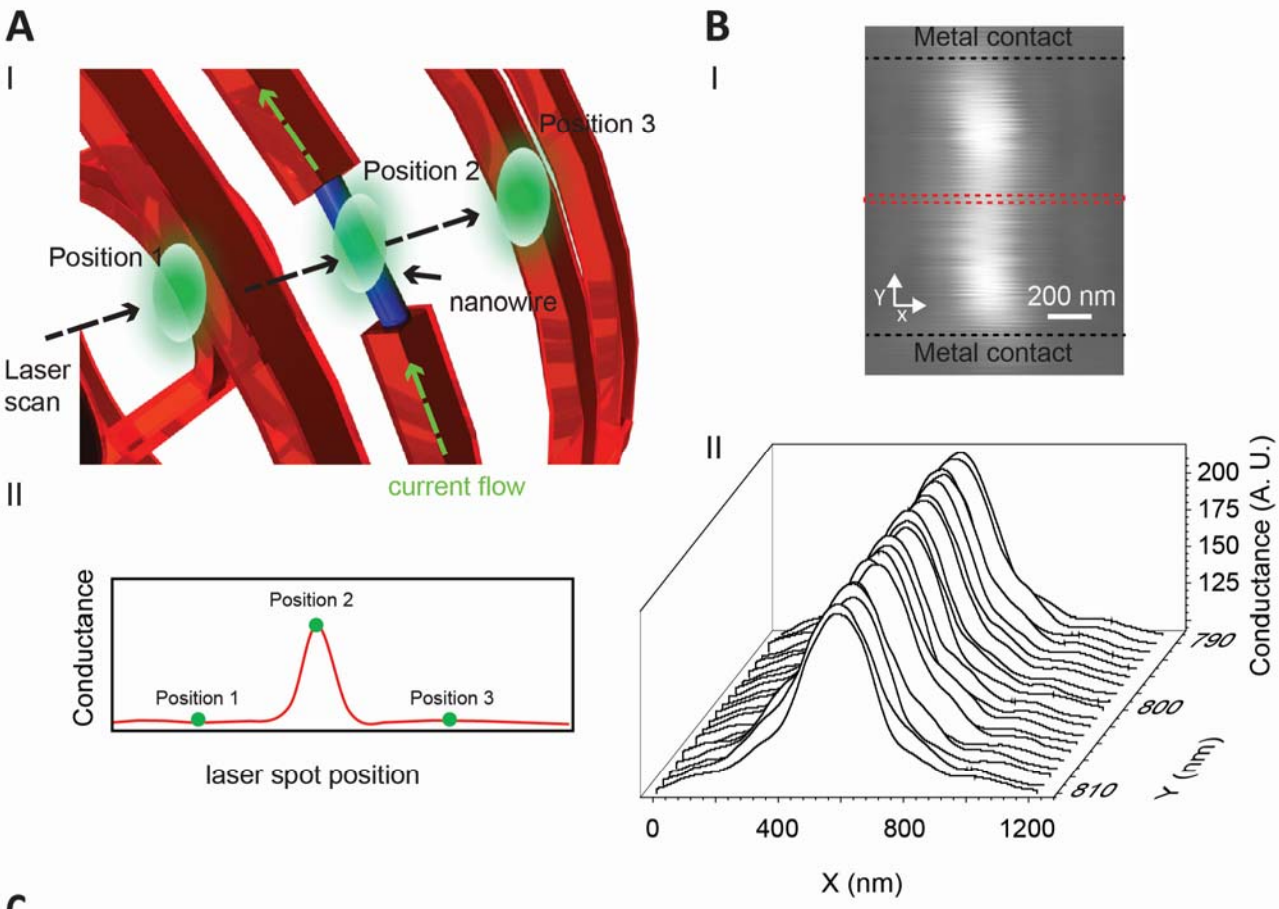
A
I
Position 3
Position 2
Position 1
nanowire
Laser
scan
current flow
II
Conductance
Position 2
Position 1
Position 3
laser spot position
B
I
Metal contact
200 nm
Metal contact
II
200
175
150
125
Conductance (A. U.)
790
800
810
Y (nm)
0
400
800
1200
X (nm)
C
I
II
65 um
10 um
5 um

Figure 3

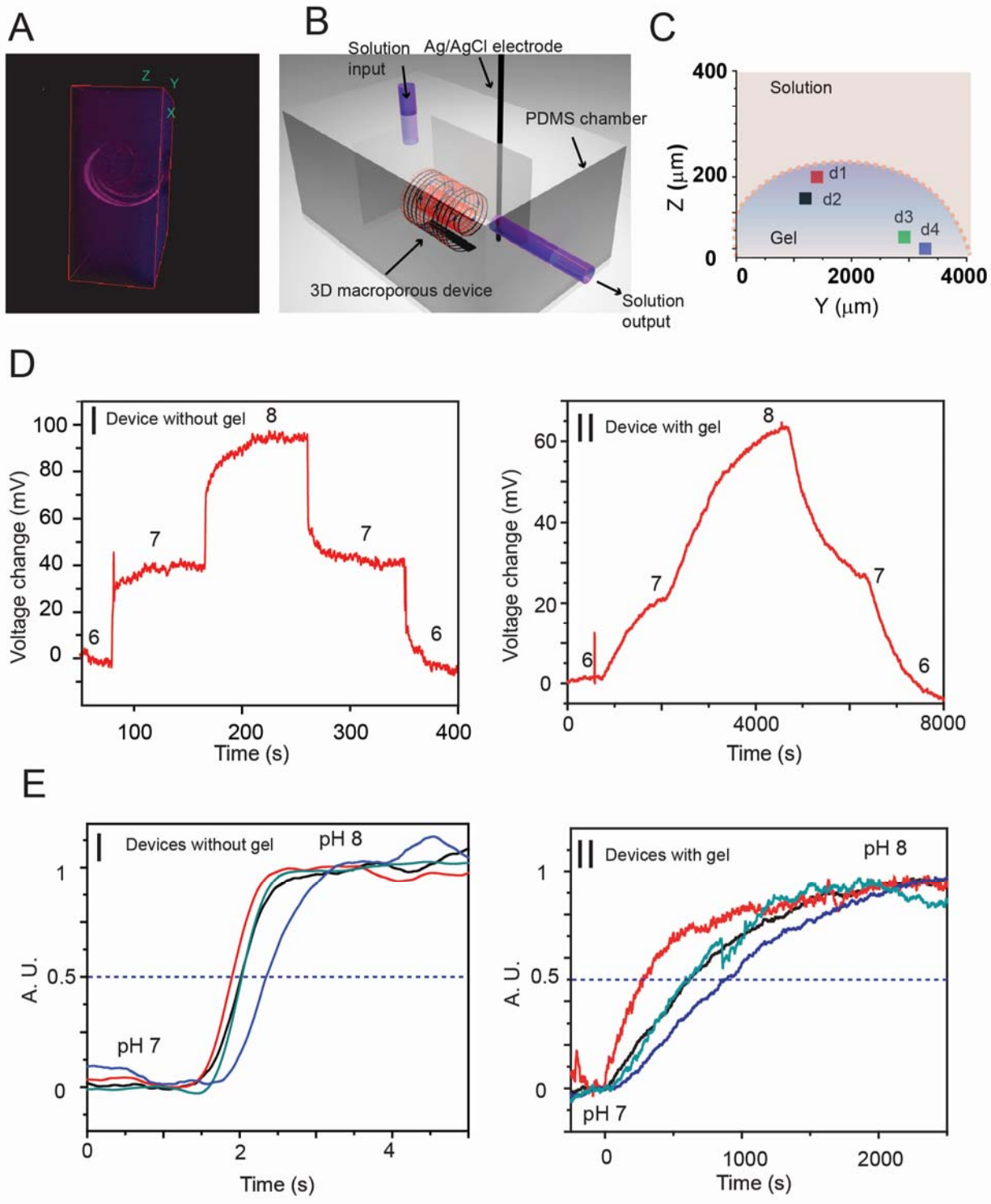
A
Z
Y
X
B
Solution input
Ag/AgCl electrode
PDMS chamber
3D macroporous device
Solution output
C
Solution
Gel
d1
d2
d3
d4
Z (μm)
Y (μm)
D
I Device without gel
II Device with gel
Voltage change (mV)
Time (s)
E
I Devices without gel
II Devices with gel
pH 8
pH 7
A. U.
Time (s)

Figure 4

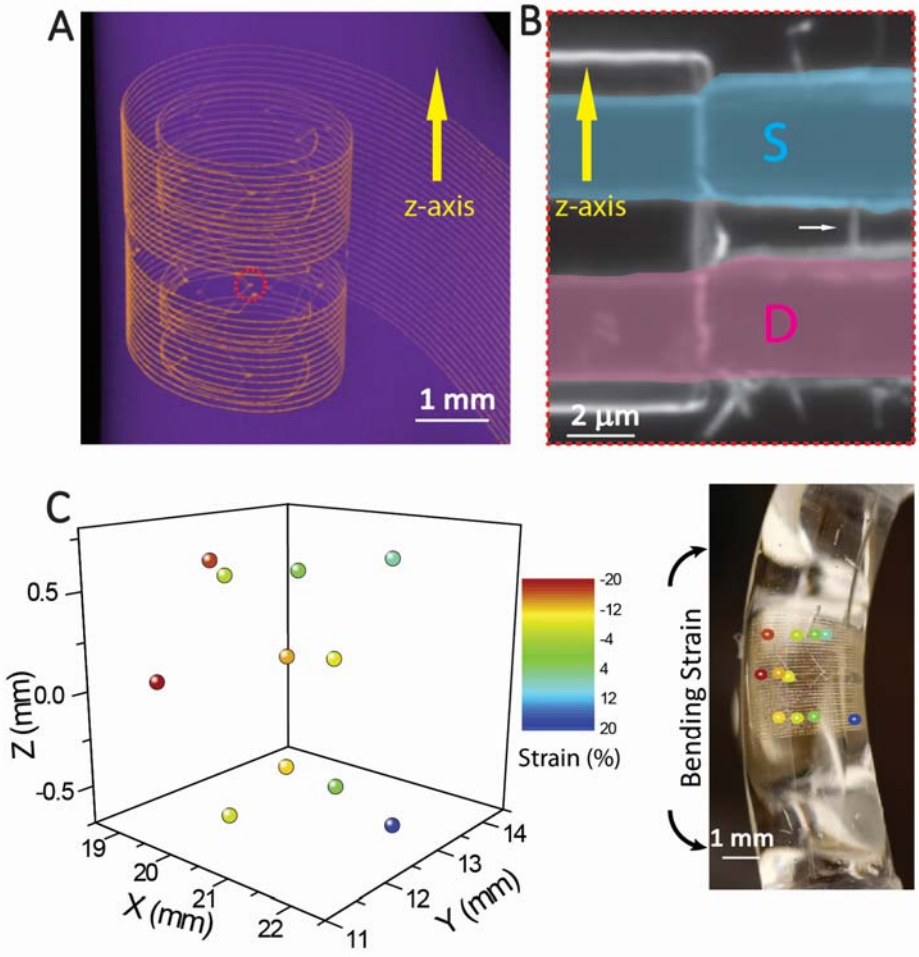
A
z-axis
1 mm
B
S
z-axis
D
2 µm
C
0.5
0.0
-0.5
Z (mm)
19
20
21
22
X (mm)
11
12
13
14
Y (mm)
-20
-12
-4
4
12
20
Strain (%)
Bending Strain
1 mm

Figure 5

Supporting Information for:

Multifunctional three-dimensional macroporous nanoelectronic networks for "smart" materials

Jia Liu, Chong Xie, Xiaochuan Dai, Lihua Jin, Wei Zhou and Charles M. Lieber

This PDF file includes:
SI text
Figures Legends S1-S5
Supplementary References

SI text

Mechanical properties. The 3D macroporous nanoelectronic networks consist of single-layer polymer (SU-8) structural and three-layer ribbon (SU-8/metal/SU-8) interconnect elements. The effective bending stiffness per unit width of the 3D macroporous nanoelectronic networks can be estimated (S1) by equation-1

$$\overline{D} = \alpha_s D_s + \alpha_m D_m \quad (1)$$

where α_s and α_m are the area fraction of the single-layer polymer and three-layer interconnect ribbons in the networks. $D_s = E_s h^3/12$ is the bending stiffness per unit width of the single-layer polymer, where E_s = 2 GPa and h are the modulus and thickness of the SU-8. For a SU-8 ribbon with 500 nm thickness, D_s is $0.02\,\mathrm{nN\cdot m}$. D_m is the bending stiffness per unit width of a three-layer structure, which includes 500 nm lower and upper SU-8 layers and 100 to 130 nm metal layer, and was measured experimentally as described below and shown in Fig. S2.

Free-standing three-layer interconnect ribbon fabrication and mechanical testing.

A Ni sacrificial layer was defined on a SiO_2/Si substrate (600nm SiO_2, *n*-type silicon 0.005 V·cm, Nova Electronic Materials, Flower Mound, TX) by EBL and thermal deposition. SU-8/metal/SU-8 elements with 100 μm long and 5 μm wide segments over the Ni-layer and wider segments directly on substrate were defined by EBL using the same approach described in *Materials and Methods*. In brief, a 500 nm thick SU-8 layer was deposited by spin coating and defined by EBL to serve as the bottom SU-8 layer. Then EBL, thermal deposition and lift-off were used to define an asymmetrical metal layer consisting of a 3 μm wide Cr/Pd/Cr (1.5/80/50 nm) ribbon centered on the bottom SU-8 element. Last, the top 500 nm thick SU-8 layer of the

SU-8/metal/SU-8 elements were defined, and then the Ni sacrificial layer was removed by Ni etchant, where the final drying step was carried out by critical point drying (Autosamdri 815 Series A, Tousimis, Rockville, MD). A schematic and an optical image of the resulting sample element are shown in Figure S2A and Figure S2B, respectively. An atomic force microscope (AFM, MFP 3D, Asylum Corp.) was used to measure force versus displacement curves for the SU-8/metal/SU-8 elements (Fig. S2A). The tip of the AFM was placed at the free end of the ribbon element and then the applied force and displacement were recorded while the AFM tip was translated down (loading) and then up (unloading), with a typical data shown in Fig. S2C. The spring constant of the AFM cantilever/tip assemblies used in the measurements were calibrated by measuring the thermal vibration spectrum (S2).

Bending stiffness analysis. Due to the residual stress, The SU-8/metal/SU-8 elements bend upward from the substrate (due to internal stress of the asymmetric metal layers) with a constant curvature, K_0, and projected length, l, where l_0 is the free length defined by fabrication. We use the curvilinear coordinate, s, to describe the distance along the curved ribbon from the fixed end, and the coordinate, x, to describe the projection position of each material point of the ribbon (Fig. S3A). For a specific material point with distance s, the projection position x can be calculated as $x = \int \cos\psi ds$, where $\psi = K_0 s$ is the angle between the tangential direction of the curvilinear coordinate s and the horizontal direction (Fig. S3B). Integration yields $x = \sin(K_0 s)/K_0$ and when $x = l$ and $s = l_0$, $K_0 = 0.0128 \mu m^{-1}$ for typical experimental parameters $l_0 = 100 \mu m$ and $l = 75 \mu m$.

As the element is deflected a distance, d, by the AFM tip with a force, F, each material point is rotated by an angle, φ, (Fig. S3B), where the anti-clockwise direction is defined as positive. Assuming a linear constitutive relation between the moment M and curvature change $d\varphi/ds$ (S3) yields

$$\frac{d\varphi}{ds} = \frac{M}{wD_m} \tag{2}$$

where M is the moment as a function of position, x (Fig. S3), and *w* is the width.

$$M(x) = -F(l - x) \tag{3}$$

Solving for the bending stiffness, D_m, with the assumption that φ is small so that $\sin\varphi \approx \varphi$ yields:

$$D_m = \frac{F}{wd}\left(\frac{ll_0\sin(K_0l_0)}{K_0} + \frac{1}{K_0{}^2}\left(l\cos(K_0l_0) - l + \frac{l_0}{2}\right) + \frac{1}{K_0{}^3}\left(\frac{\sin(2K_0l_0)}{4} - \sin(K_0l_0)\right)\right) \tag{4}$$

The slope of a representative loading force-deflection curve, yields $F/d = 12\text{nN}/\mu\text{m}$ (Fig. S2C), and using equation-4 the calculated bending stiffness per width (w = 5 μm) is $D_m = 0.358\text{nN}\cdot\text{m}$. For typical 3D macroporous nanoelectronic networks the area fraction for both types of elements (i.e., SU-8 and SU-8/metal/SU-8) can range from 1 –10%, yielding values of the effective bending stiffness from 0.0038 to 0.0378 $\text{nN}\cdot\text{m}$.

Supplementary Figure Legends:

Fig. S1. 2D macroporous nanoelectronic network. Zoom-in of the region enclosed by the white-dashed box in Fig. 2*D*. The white arrows highlight several wire bonds.

Fig. S2. Bending stiffness measurements. (*A*) Schematic illustrating the measurement of the bending stiffness of a representative SU-8/metal/SU-8 element in the macroporous nanoelectronic networks. EBL is used to define substrate-fixed and substrate free beams, where internal stress in the central metal layer causes the structure to bend-up upon relief from the substrate (*SI text*). The tip of the AFM is placed at the free end of the ribbon, and then translated vertically downward (loading) and upward (unloading) to yield the force-displacement curves. In the scheme, w: the width of the ribbon, l_0: the length of the ribbon, l: the projected length of the ribbon, and d: the displacement of the AFM tip. (*B*) Optical micrograph of the fabricated structural element, where the substrate fixed portion is highlighted by the red dashed rectangle and the free beam is in the upper portion of the image with a width of 5 μm and a length of 100 μm. (*C*) A typical force – displacement curve with F / d for loading and unloading of 12 and 10.5 nN/μm, respectively. Similar deviation between the loading and unloading has been attributed to inelastic deformation (S4, S5); hence, we use the larger loading value in calculations to provide an upper limit.

Fig. S3. Schematic for calculations. (*A*) A schematic of the position of the substrate free beam before (black) and after (red) applying a calibrated force, F, and vertical displacement, d, at the end of the beam with the AFM. (*B*) The angle between the tangential direction of a material point

on the beam and the horizontal direction, ψ , of the ribbon before (black) and after displacement, $\psi + \varphi$, (red). l_0: the total length of the ribbon. *l:* projection of the ribbon.

Fig. S4. Localization of 3D macroporous nanoelectronic devices. 3D macroporous nanoelectronic FET devices exhibit photoconductivity (S6) that was used to determine spatial positions using a confocal microscope equipped with an analog signal input box (see *Materials and Methods*). *(A)* Schematic of photocurrent detection and correlation with confocal microscopy laser spot scanning position. A 405 nm laser wavelength, 100X water immersion lens, and 0.1 mV source/drain device bias-voltage were used in the experiments. (*B*) High-resolution (1 nm per pixel) photocurrent image (*I*) from a single nanowire device (2 μm channel length between upper/lower metal contacts) recorded scanning in x-y plane. The red dash line indicates the direction perpendicular to the nanowire axis. The black dash lines indicate the boundaries of metal contacts. (*II*) Photocurrent measured along the red dash line in (*I*). Experimental data are fit with a Gaussian distribution (red solid curve). (*C*) Distribution of the center point positions determined from the 20 independent scans in region of indicated in Fig. 3*B* and about the single scan line shown in (S4B).

Fig. S5. Calibration of the 3D macroporous nanoelectronic strain sensors. (*A*) Conductance change versus time as a 10% tensile strain was applied to hybrid 3D macroporous nanoelectronic networks/PDMS cylindrical sample. The downward and upward pointing arrows denote the times when the strain was applied and released, respectively. The direction of strain on the cylindrical hybrid sample and projected position of the macroporous nanoelectronic networks are

indicated in the right optical micrograph. The conductance changes of 11 measured nanowire devices (labeled arbitrarily in terms of increasing sensitivity) were recorded and used for the conductance change per strain calibration. (*B*) Strain sensitivity calibration of the nanowire devices is plotted in 3D. The data points are color coded by the sensitivity of the devices (*A*).

Supplementary References:

S1. Kim DH, et al. (2011) Epidermal electronics. *Science* 333:838-843.

S2. Butt HJ, Jaschke M (1995) Calculation of thermal noise in atomic force microscopy. *Nanotechnol* 6:1-7.

S3. Landau LD, Lifshitz EM (1986) *Theory of Elasticity, 3rd edition*, p67-73. (Elsevier).

S4. Feng R, Farris R (2002) The characterization of thermal and elastic constants for an epoxy photoresist SU8 coating. *J Mat Sci* 37:4793-4799.

S5. VanLandingham M, Villarrubia J, Guthrie W, Meyers G (2001) *Nanoindentation of Polymers: An Overview. Macromol Symp* 167:15-43.

S6. Ahn Y, Dunning J, Park J (2005) Scanning photocurrent imaging and electronic band studies in silicon nanowire field effect transistors. *Nano Lett* 5:1367-1370.

Figure S1

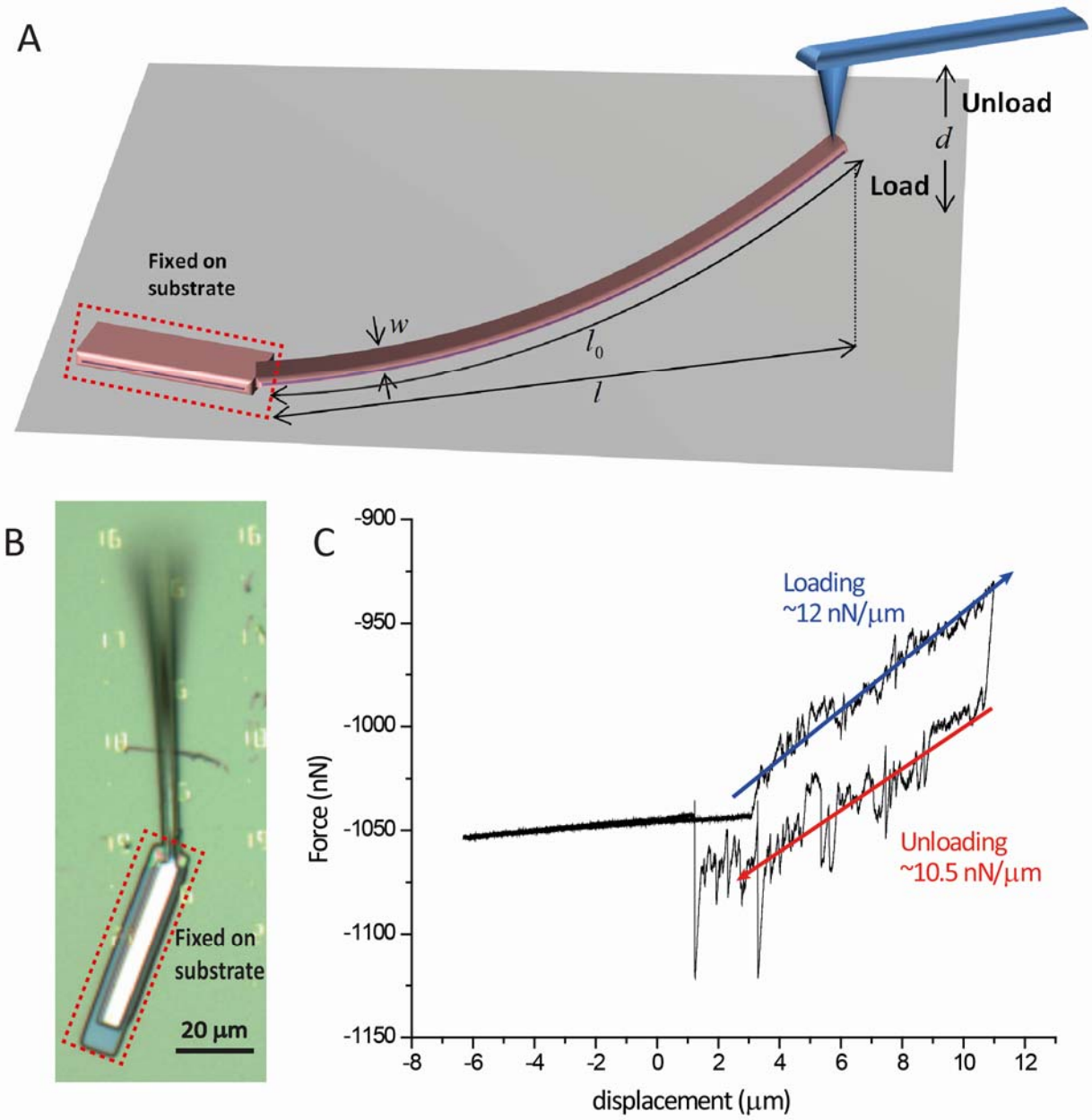
A
Unload
d
Load
Fixed on
substrate
w
l_0
l
B
Fixed on
substrate
20 μm
C
Loading
~12 nN/μm
Unloading
~10.5 nN/μm
Force (nN)
displacement (μm)
-900
-950
-1000
-1050
-1100
-1150
-8
-6
-4
-2
0
2
4
6
8
10
12

Figure S2

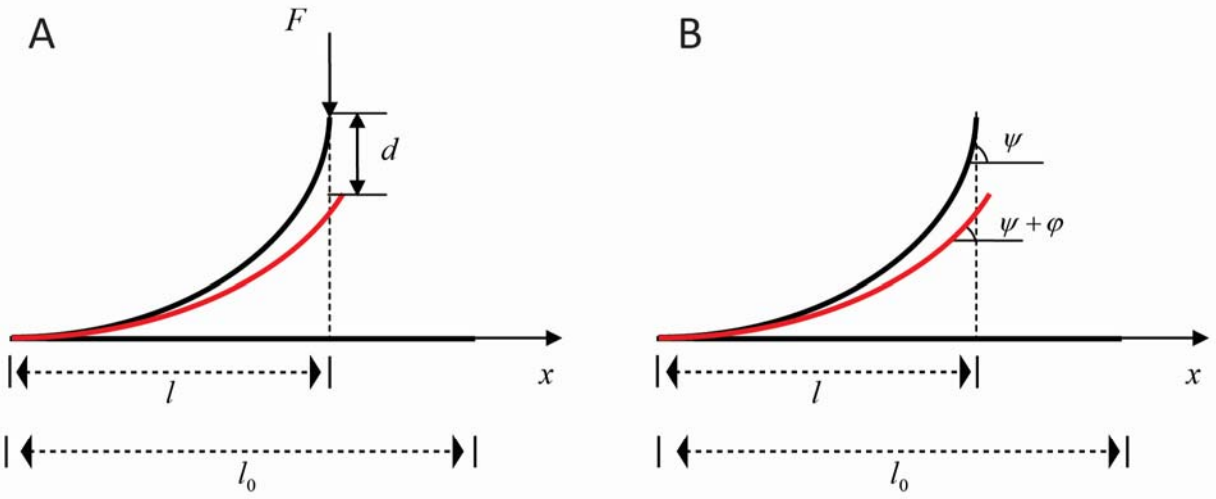

Figure S3

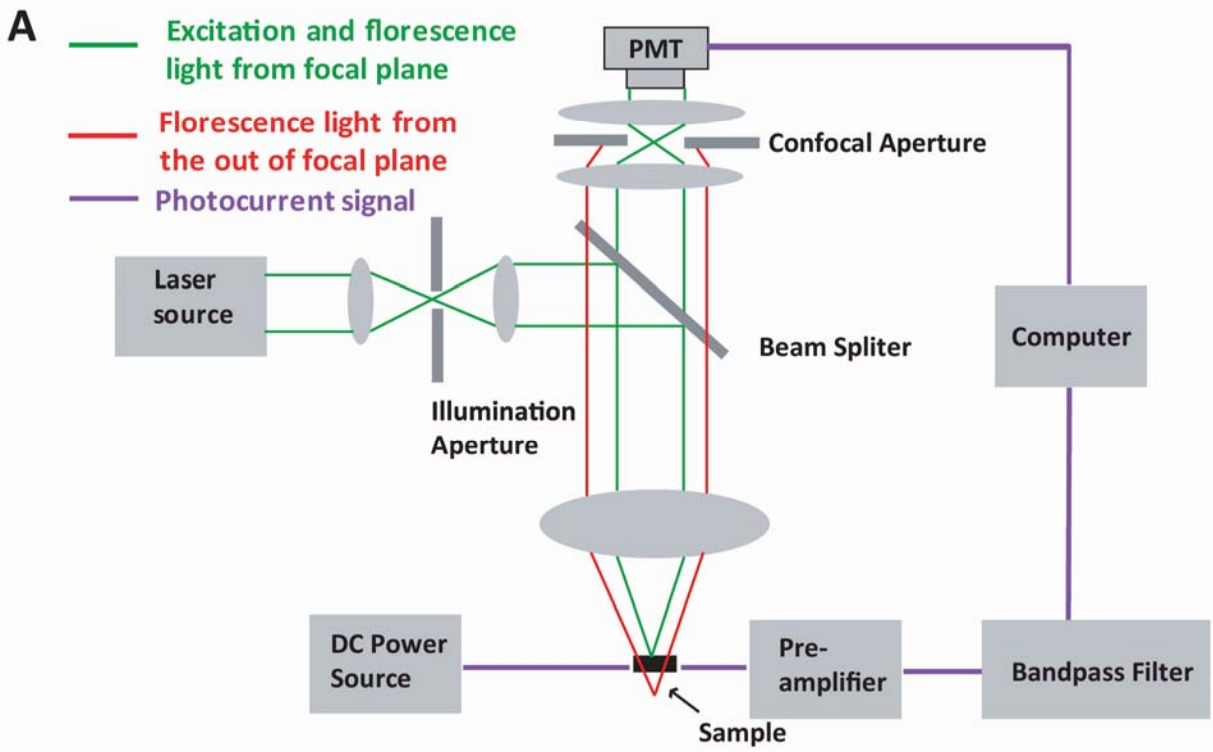
A
Excitation and florescence light from focal plane
Florescence light from the out of focal plane
Photocurrent signal
PMT
Confocal Aperture
Laser source
Beam Spliter
Computer
Illumination Aperture
DC Power Source
Pre-amplifier
Bandpass Filter
Sample

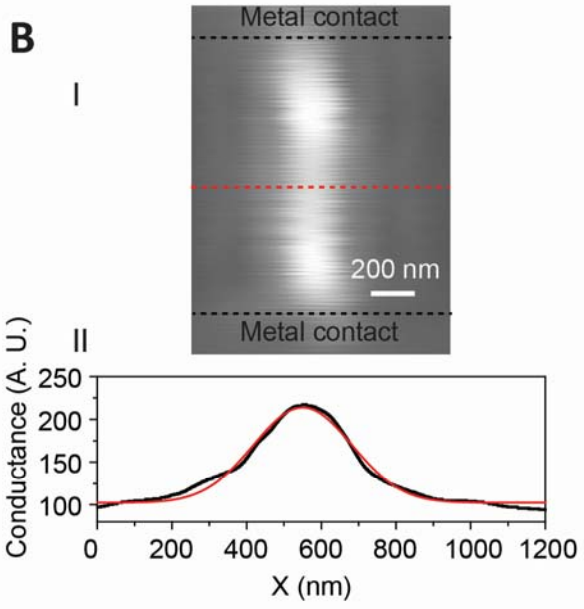
B
I
Metal contact
200 nm
Metal contact
II
Conductance (A. U.)
250
200
150
100
0
200
400
600
800
1000
1200
X (nm)

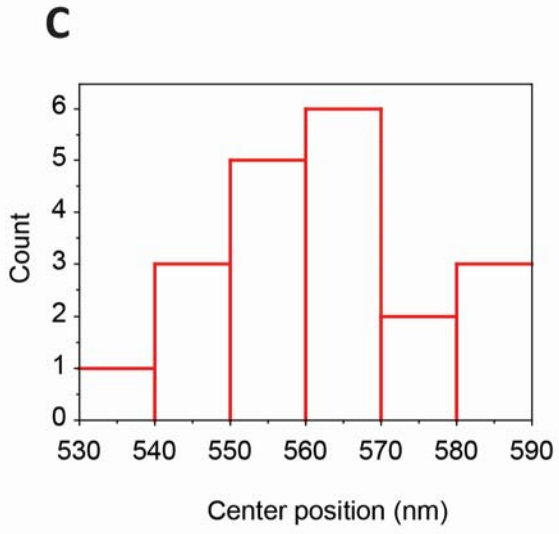
C
Count
6
5
4
3
2
1
0
530
540
550
560
570
580
590
Center position (nm)

Figure S4

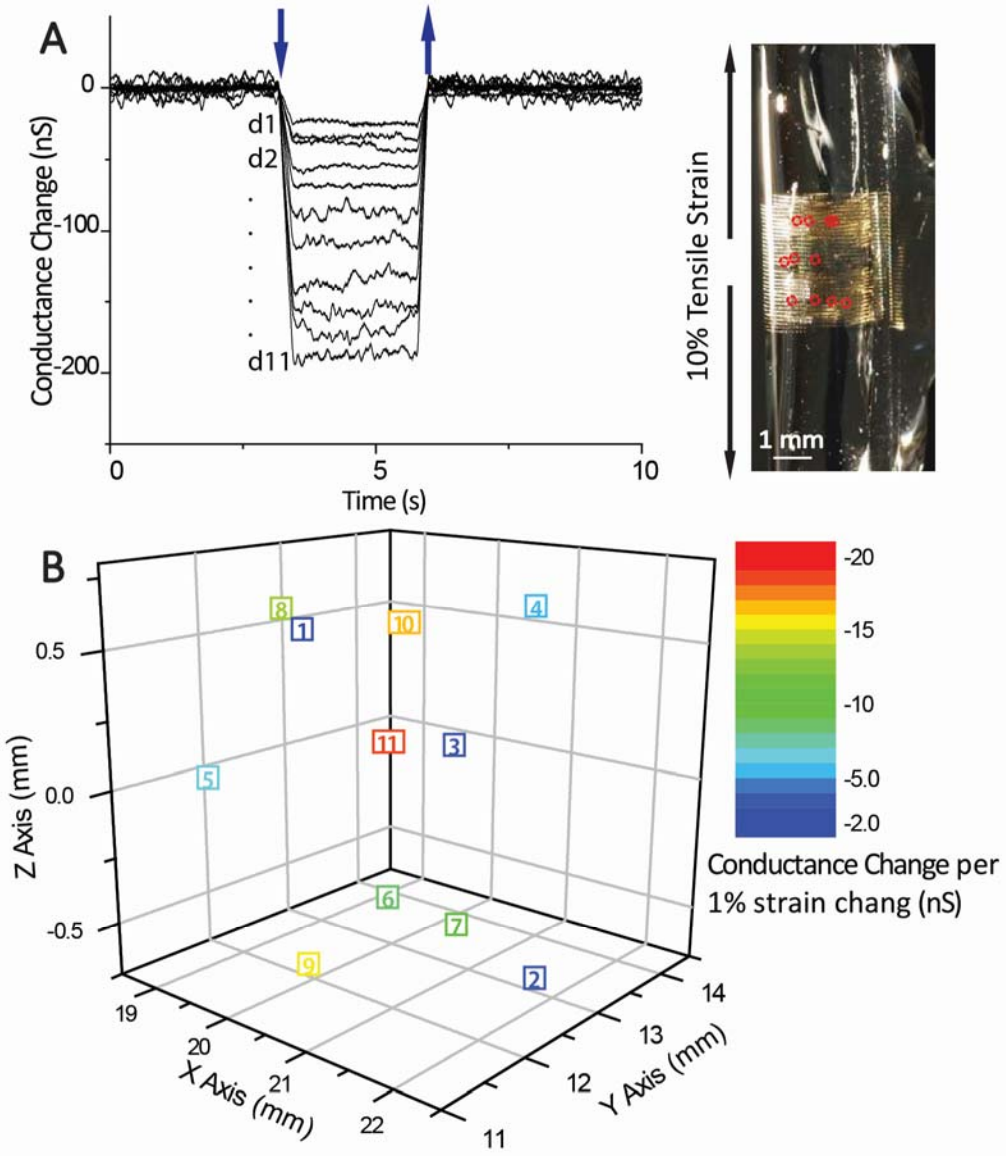
A
0
-100
-200
Conductance Change (nS)
d1
d2
d11
0
5
10
Time (s)
10% Tensile Strain
1 mm
B
0.5
0.0
-0.5
Z Axis (mm)
8
1
10
4
11
3
5
6
7
9
2
19
20
21
22
X Axis (mm)
14
13
12
11
Y Axis (mm)
-20
-15
-10
-5.0
-2.0
Conductance Change per
1% strain chang (nS)

Figure S5